Journal of Design Against Fatigue
https://minerva-aset.com/JDAF

MINERVA ASET

# Track-scale Anisotropic Thermal Material Model as a Viable Substitution in Selective Laser Melting

Pouria Deldar Masrour[1*], Reza Tangestani[2], Gholamhossein Farrahi[1], Étienne Martin[3], Lang Yuan[4], Tianyu Zhang[4]

[1]*Department of Mechanical Engineering, Sharif University of Technology, Tehran, Iran*
[2]*Department of Mechanical and Mechatronic, University of Waterloo, Waterloo, ON, Canada*
[3]*Depatment of Mechanical Engineering, Polytechnique Montréal, QC, Canada*
[4]*Department of Mechanical Engineering, University of South Carolina, Columbia, SC, United States*

*P A P E R  I N F O*

*Paper history:*
Received 4 October 2023
Received in revised form 11 October 2023
Accepted 12 October 2023

*Keywords*:
*SLM*
*FEM*
*Anisotropic Conduction*
*Track-scale*
*Melt pool*
*Cooling rate*

*A B S T R A C T*

High temperature gradients and resulting residual stresses are the main sources of defects such as cracks, distortion and fatigue failure is selective laser melting. In this paper, a new material model utilizing anisotropic thermal conduction model and track-scale heat input model is used to predict the melt pool geometry, material state and thermal history during the SLM process of SS316L in a large range of laser parameters. The model takes into consideration both the material state and the issue of phase transition during the track-scale simulation. The simulated melt pools in the beam-scale and track-scale simulations are compared with experimental measurements in different laser parameters. It is found that the proposed material model is able to maintain accuracy between the beam-scale and track-scale simulations at an average of 5μm regarding melt pool dimensions. Furthermore, it can be inferred that both track-scale and beam-scale models exhibit the capability to provide precise predictions of melt pool geometries when compared to experimental measurements while the former being about 100 times faster than the latter. An average error of 10% was concluded for the material state comparison of the two models while the track-scale model was able to capture the temperature profile and cooling rate accurately in comparison with the beam-scale model.

## 1. INTRODUCTION

Additive manufacturing (AM) represents an innovative manufacturing process in contrast to the traditional subtractive manufacturing methods which allows for the production of components based on a CAD file, eliminating the need for dedicated tools or dies. Selective Laser Melting (SLM) is a widely employed laser powder bed fusion process capable of meeting the precision demands of advanced applications in industries such as aerospace, defense, and biomedical fields [1, 2]. In recent times, there have been numerous research endeavors aimed at improving the performance and capabilities of parts fabricated using SLM. These investigations mostly focus on process parameters optimization [3, 4], thermal behavior [5-7] and post processing [8, 9]. Additionally, the research focus has been expanded to explore the microstructure in order to achieve enhanced material properties. [10-12]. However, high-temperature gradient, and as a result high cooling rate, during the SLM process tend to induce high thermal stresses. Thermal stress-induced flaws, such as cracks, fatigue-related failure and delamination, represent the primary causes of failure in the printing process [13-16].

To resolve the high temperature gradient during the SLM process, Simons et al. [17] and Hussein et al. [18] optimized the process parameters to minimize the temperature gradient by conducting a large experimental data base. This method is not viable for the cost to conduct such experiments is too high. Therefore finite element (FE) method has been widely used to predict the thermal and behavior during and post process [19, 20].

Understanding the solidification behavior in the SLM process relies on the assessment of crucial factors such as melt pool morphology, track surface features, and thermal evolution. [18, 21, 22]. Different models have been developed. Yuan P. et al. [23] found out the melt pool takes a wide and shallow shape in presence the Marangoni effect while it takes a narrow and deep shape in absence of the Marangoni effect. The study utilized isotropic physical properties. Among the various properties, thermal conductivity plays a pivotal role in influencing the geometry of the melt pool. A number of investigations have been carried on the anisotropic enhanced thermal conductivity. Kamara A. M. et al. [24] found that employing anisotropically enhanced model can enhance the accuracy of melt pool dimension predictions during the laser deposition of nickel alloys. Safdar et al. [25] used the

*Corresponding Author Email: pourya.deldar@mech.sharif.edu (Pouria Deldar Masrour))

Please cite this article as: P.D. Masrour, R. Tangestani, G.H. Farrahi, É. Martin, L. Yuan, T. Zhang, Track-scale Anisotropic Thermal Material Model as a Viable Substitution in Selective Laser Melting, ***Journal of Design Against Fatigue,*** Vol. 1, No. 3, (2023), 19-33

anisotropic approach to artificially simulate melt pool convection for laser melting of Inconel 718. Siao et al. [26] found that utilizing the anisotropic heat conduction leads to small deviation in the melt pool dimensions compared to the experimental measurements in comparison with the Marangoni flow model.

The numerical models of the SLM process are usually categorized into three levels: micro-level models which are in the range of a few hundred microns, meso-scale models which are in the range of a number of scanning tracks and macro-level models which simulate the whole part. Depending on the scale of the simulation, various heat input models can be employed, including beam-scale, track-scale and layer-scale [27]. One common way to simulate the process in macro-scale level is to use the lumped laser model where heat input is implemented over several layers. This approach although offers acceptable accuracy predicting part distortion, lacks resolution for predicting thermal history in the model [28, 29]. FE model utilizing beam-scale heat input, is well-suited for simulating the temperature changes within a single welding track or several tracks. However, it is not conducive to simulating a component-scale model comprising multiple layers, each with several laser tracks, due to the substantial computational overhead involved. [30]. This is due to small diameter of laser and large size of the building part. To solve a transient beam-scale model, a large number of finite elements and time increments is needed [31]. Researchers have reported a computational time of 90h for the thermal model [32].

A conventional way to make the model more efficient, is the use of track-scale heat input model. In this model, the beam-scale heat input is integrated over an arbitrary time increment and then the entire track length is simulated in a single increment. This will decrease computational time drastically for the time increment can be set as a factor of the laser radius. Irwin et al. [31] used a 3D Goldak track-scale heat input model which could predict the distortion within the component with a precision of 10%. They report a computational reduction by factor of 100. Luo et al. [30] developed a 2D Gaussian track-scale input to predict temperature field during SLM of SS316L which reduce computational time by 70%. The model has a 10% precision for predicting the temperature field while having an error of 10 ~25% for molten pool dimension prediction. Tangestani et al. [33] developed a 3D exponentially-decaying track-scale model for LPBF process to consider the depth to which heat penetrates within the powder. The model accounts for the effect of powder state during the simulation. They report a computational reduction by factor of 300 and higher. Also, a deviation of 5μm predicting the melt pool depth and a 5% error while predicting the temperature distribution below the solidus temperature was reported.

Although the model developed by Tangestani et al. [33] uses an isotropic thermal conduction, it still lacks the precision to accurately predict the melt pool dimensions specially the width. On top of that the material state transition problem during the track-scale model has not been addressed practically. Additionally, to the writer's knowledge the track-scale model has not yet been used in conjunction with the anisotropic thermal conduction model to predict the thermal history and the melt pool dimensions.

The primary objective of this paper is to create a track-scale model incorporating the anisotropic thermal conduction model. This model aims to strike a balance between efficiency and accuracy, allowing for the prediction of thermal histories and melt pool dimensions across a wide range of process parameters. A practical solution to the track-scale phase transition problem is provided. Calibration method of the anisotropically enhancement factors based on the laser parameters is presented. In the end, an analysis is conducted on the predicted molten pool geometries, nodal temperatures, and cooling rates.

## 2. EXPERIMENTAL METHODOLOGY

### 2.1. MATERIAL COMPOSITION

This research utilizes commercial gas-atomized 316L stainless steel powder supplied by Carpenter Technology Corporation. The powder exhibits a particle size distribution ranging from 15 to 45μm, with an average size of 30μm. A relative density of 0.6 was considered for the powder. The nominal composition of the powder is **17.7% Cr**, **12.7% Ni**, **2.36% Mo**, **0.65% Mn**, **0.62 Si**, **0.1% N**, **0.03% O**, **0.022% C**, **0.02% Cu**, **0.007% P**, **0.005% S** and the balance is **Fe**. The powder used is shown in **Figure 1-(a)**. The picture was taken using Tescan Vega3 SEM.

### 2.2. EXPERIMENTAL PROCEDURE

To verify the material model's accuracy, a series of Design of Experiment (DOE) trials were performed. The DOE was executed using the Aconity MIDI system, which is equipped with a single-mode fiber laser capable of delivering a maximum laser power of 1000W. In order to verify the heat transfer model's accuracy, a sequence of individual tracks was printed onto a 10mm x 10mm x 10mm plate using SS316L powder. 30 distinct process parameter combinations were used to print a total of 150 single tracks on a 30μm powder layer thickness. To minimize procedure error, the experiment was run five times for each set of process parameters. Laser power and speed were the investigated parameters in the mentioned DOE. The laser power was adjusted within the range of 80W to 800W, while the laser speed spanned from 160mm/s to 4,000mm/s.

### 2.3. EXPERIMENTAL MEASUREMENT

To be able to validate the simulations with experiment, melt pool geometries formed during the single tracks need to be investigated. To do so, cross sectional area of the single tracks is observed under an optical microscope where the dimensions are measured. The measurements were competed using Keyence VHX-5000. The cross sections are ground and polished before the observation. The extent of intrusion into the pre-existing solidified substrate is referred to as depth, while the separation between the two extremities is termed width. **Figure 1-(b)** shows a cross sectional view of the melt pool and the dimension measurement.

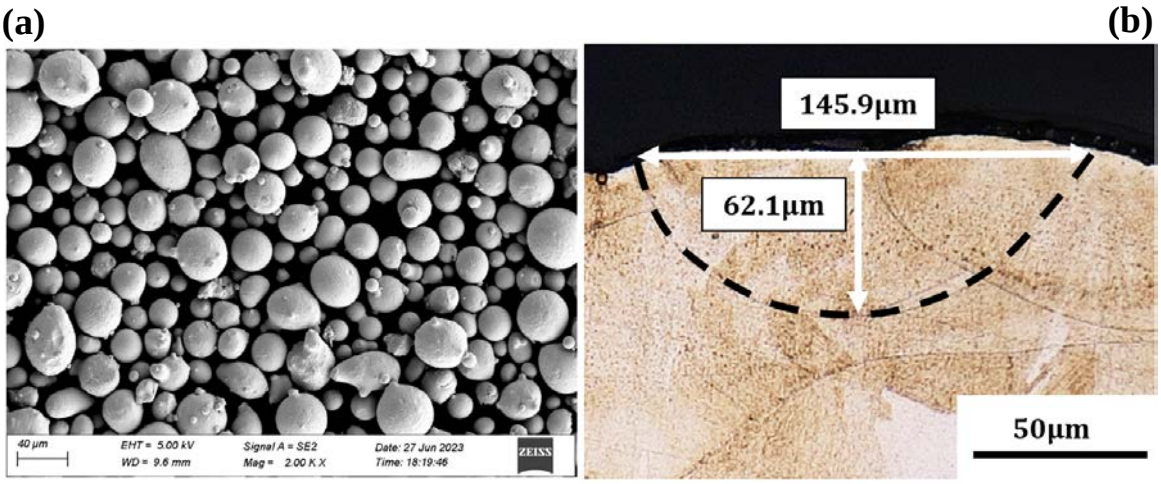


**Figure 1. (a)** SS316L powder used for fabrication **(b)** melt pool geometry and dimension measurement.

## 3. Heat Transfer Model

The governing equation employs the 3D transient heat transfer equation given by Fourier series which is stated as **Eq.1** [34].

$$\frac{\partial}{\partial x}\left(k_x \frac{\partial T}{\partial x}\right)+\frac{\partial}{\partial y}\left(k_y \frac{\partial T}{\partial y}\right)+\frac{\partial}{\partial z}\left(k_z \frac{\partial T}{\partial z}\right)+Q=\rho C\frac{\partial T}{\partial t} \quad (1)$$

Where $k_x$, $k_y$ and $k_z$ represent the thermal conductivities along their respective directions, ρ denotes density, C indicates specific heat, T is Temperature, t signifies time and Q is the internal heat generation per unit volume.
Convective heat losses were considered as shown in **Eq.2**.

$$Q_c = h_c(T - T_0) \quad (2)$$

Where $h_c = 15\ \mathrm{W/m^2}$, is the convective heat transfer coefficient.
Radiative heat losses were accounted for using Stefan-Boltzmann law presented in **Eq.3**.

$$Q_r = \sigma\varepsilon(T^4 - T_0^4) \quad (3)$$

Where $\sigma = 5.67 \times 10^{-8}\ \mathrm{W/m^2K^4}$ represents the Stefan-Boltzmann constant and $\varepsilon = 0.5$ denotes the emissivity. $T_0$ in **Eq.2** and **Eq.3** is the ambient temperature (25°C).

### 3.1. LASER HEAT SOURCE MODELING

In order to achieve precise simulation of the LPBF process, a material model capable of replicating the phase transitions from powder to liquid and from liquid to solid states is mandatory. Furthermore, capturing the heat input characteristics accurately is essential for reaching acceptable results. This paper employs two distinct heat source models to strike a balance between precision and effectiveness which are the exponentially decaying and the track-scale models which we will refer to them as ED and HL model for convenience. First the ED model is presented as a reference for calibrating the HL model which will then be used to reach more time efficient simulations while having acceptable precision.

#### 3.1.1. ED HEAT SOURCE MODEL

In this model, the laser's thermal energy input is depicted as a heat source having a Gaussian distribution that progressively diminishes as it moves through the depth of the powder. The energy input is described in **Eq.4** [33].

$$Q = \frac{2P}{\pi r_l^2} e^{\left(-2\frac{x^2+y^2}{r_l^2}\right)} \frac{\eta}{H} e^{-\left[\frac{|z|}{H}\right]} \quad (4)$$

Where Q is the input energy, η represents the absorption coefficient, and P denotes the laser power. *x*, *y*, and *z* represent the local coordinates. $r_l$ is the laser radius. The energy penetrated through the powder is determined using the H parameter which is equal to the powder layer thickness [35].

#### 3.1.2. HL HEAT SOURCE MODEL

In the HL model, the ED heat input is integrated across a time step. As a result, **Eq.5** is formed.

$$\bar{Q} = \frac{1}{\Delta t}\int_{t_0}^{t_0+\Delta t} Q\,dt \quad (5)$$

where $\Delta t$ indicates time increment, $t_0$ denotes time at beginning of the increment and Q represents heat input model of the beam-scale source. Upon substituting **Eq.4** into **Eq.5**, the resulting expression for the moving HL heat input in the x-direction, aligned with the laser scanning direction, is as follows [33]:

$$Q = C\frac{P\eta}{\sqrt{2\pi}\Delta t v_s H r_l} e^{\left(-\left[\frac{|z|}{H}\right]-2\left(\frac{y}{r_l}\right)^2\right)}\left(\mathrm{erf}\left(\frac{\sqrt{2}(x_{end}-x)}{r_l}\right)-\mathrm{erf}\left(\frac{\sqrt{2}(x_{start}-x)}{r_l}\right)\right) \quad (6)$$

Where the erf corresponds to the error function. $x_{start}$ and $x_{end}$ denote the initial and final positions of the laser in the beginning and end of the increment and $\Delta t$ is the time increment. The "C" parameter needs to be calibrated based on the ED model for the use of track-scale heat input model will cause the thermal history to drop as discussed by Tangestani et al. [33]. Utilizing a track-scale heat input model, as highlighted by researchers, would result in a notable reduction in computational time [31, 33].

### 3.2. FINITE ELEMENT MODEL IMPLEMENTATION

The heat transfer analysis is carried out using ABAQUS, a commercial finite element software. The two heat input models are incorporated into ABAQUS through the utilization of the DFLUX subroutine which applies the heat flux in accordance with **Eq.4** and **Eq.6** based on the spatial position of the laser at every increment. A domain measuring 2mm x 0.25mm x 0.5mm is established to assess the melt pool dimensions formed in single track simulations for both the ED and HL heat input models. Only half of the geometry is modeled utilizing symmetry for computational efficiency. The dimensions are chosen such that stable melt pools could be formed during the simulation and the layer thickness was fixed at 30µm. The part is meshed using DC3D8 elements for the entire geometry. The model uses a mesh algorithm for further computational efficiency. The regions closely interacting with the laser are discretized with elements of dimensions measuring 25µm along the x-direction, 10µm along the y-direction, and 10µm along the z-direction and the element dimensions in the coarser regime are 100µm, 40µm and 95µm respectively. **Figure 2** shows a view of the single-track model used for melt pool dimension determination for different process parameters and heat input models.

### 3.3. MATERIAL PROPERTIES

To take the phase transition during the SLM process into account, temperature and state properties are employed for both solid and powder state.
**Eq.7** is used to relate the thermal conductivity of powder and solid state as a function of porosity [34].

| | |
|---|---|
| $k_p=(1-\varphi)^4 k_s$ | (7) |

Where $k_p$ and $k_s$ represent thermal conductivities of the powder and solid state, and $\varphi$, is porosity. Similarly, **Eq.8** illustrates powder and solid phase density dependence on porosity.

| | |
|---|---|
| $\rho_p=(1-\varphi)\rho_s$ | (8) |

Where $\rho_p$ and $\rho_s$ denote densities of powder and solid state, and $\varphi$, is porosity.
Properties of SS316L is illustrated in **Figure 3**. As shown in **Figure 3-(b)**, specific heat is the same for both states because it has no dependance on mass whereas thermal conductivity relies heavily on the porosity of the powder. Therefore, both values for powder and solid state are plotted for easier use in **Figure 3-(a)**. The density values are presented only for the solid state.
Additionally, the sudden rise in specific heat capacity between solidus and liquidus temperatures, caused by latent heat is replaced with a gradual increase above the melting temperature (1372°C) to avoid convergence failure during the analysis while keeping acceptable temperature history predictions.
To improve the accuracy of melt pool dimension predictions, it is imperative to consider the impact of melt pool convection induced by Marangoni flow.
Anisotropically enhancement thermal conductivity method can be employed to replicate convection during laser melting which can be expressed as **Eq.9** [25].

| | |
|---|---|
| $k_x = \psi_x k\ ,\ k_y = \psi_y k\ ,\ k_z = \psi_z k$ | (9) |

Where $\psi_x$, $\psi_y$, $\psi_z$ are the enhancement factors of thermal conductivity $k$. It's been well established these factors are dependent on laser parameters as well as temperature shown in **Eq.10** [36].

| | |
|---|---|
| $\begin{cases} \psi_x,\psi_y,\psi_z=1, & T<T_{melting} \\ \psi_x=1,\ \psi_y=f_y(P,v),\psi_z=f_z(P,v), & T\geq T_{melting} \end{cases}$ | (10) |

The subsequent equation asserts that the powder and solidified material states remain unaffected by the anisotropically enhancement factors, and thermal conduction remains consistent in all directions. However, the thermal conductivity of the liquid state is heightened when fluid flow is present. The enhancement is present in width and depth directions. Thermal conduction along the length direction is kept unchanged.
The following equations have been adapted from Zhang et al. [36] for anisotropically enhanced coefficients. **Eq.11** shows the relation of the depth factor.

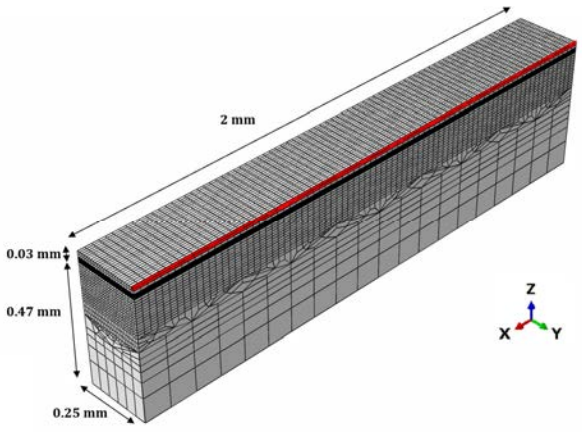


**Figure 2.** The 3D model of single track. Powder layer thickness is 0.03mm and the substrate has a 0.47mm thickness. The line shown in the figure shows the laser scanning direction.

$$\psi_z = a_1 \frac{P}{\sqrt{v}} + b_1 \quad (11)$$

The laser speed has a more pronounced impact on the melt pool width. **Eq.12** illustrates the relation of the width factor.

$$\psi_y = \begin{cases} a_2 v + b_2, & v \le v_a \\ 1, & v > v_a \end{cases} \quad (12)$$

In the following equations $a_1$, $b_1$, $a_2$, $b_2$ and $v_a$ are coefficients which must be determined after calibrating the model using experimental evaluation. **Eq.12** is independent of laser power, in contrast to **Eq.11**, which does not account for the expected influence of laser power on the melt pool width. This is due to small range of laser power (50 Watts) studied in the work conducted by Zhang et al. [36] which is not the case in the following research. To address this problem, **Eq.12** is defined in discrete laser power values base on experimental data. Interpolations will then be used to calculate general factors for general laser parameter values.

### 3.3.1. ANISOTROPIC COEFFICIENTS CALIBRATION

To calibrate the anisotropic coefficients, the 30 experimental data sets are classified into two groups. The 1st set include process parameters having constant laser energy density which consists of 20 data sets. The 2nd set includes process parameters having constant laser speed which consists of 10 data sets. The 1st data set will be used to calibrate the anisotropic heat conduction model. The 2nd data set will then be used to validate the calibrated model.

In order to establish model calibration, the anisotropically enhanced factors are initially adjusted empirically to achieve the closest agreement between the molten pool dimensions generated in the simulation and the corresponding experimental data. Once the validity of the results has been verified, the coefficients are fit according to the initially defined functions (**Eq.11** & **Eq.12**). **Figure 4-(a)** and **Figure 4-(b)** show the obtained curves along depth and width directions. **Table 1** shows the values obtained for the coefficients in **Eq.11** & **Eq.12**. five sets of coefficients have been presented for the five curves available for the width direction and one set of coefficients has been presented for the depth direction.

### 3.4. MATERIAL SATE TRANSITION

Throughout the SLM process there is a continuous state transition occurring among powder, solid, and liquid phases which are all modeled separately in the developed model. To incorporate the state transition and anisotropically enhanced thermal conduction, UMATHT subroutine is used in ABAQUS.

The state of material is controlled using an index. If the index attains a value of zero, it signifies that material is in powder state, whereas an index value of one indicates that material is in either solid or liquid state. Properties is then chosen respectively.

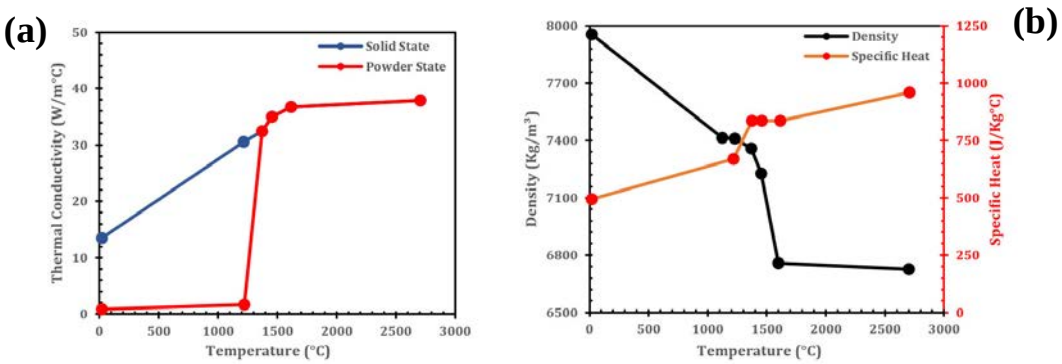


**Figure 3.** Temperature dependent properties. **(a)** Thermal conductivity **(b)** Specific heat and density [34].

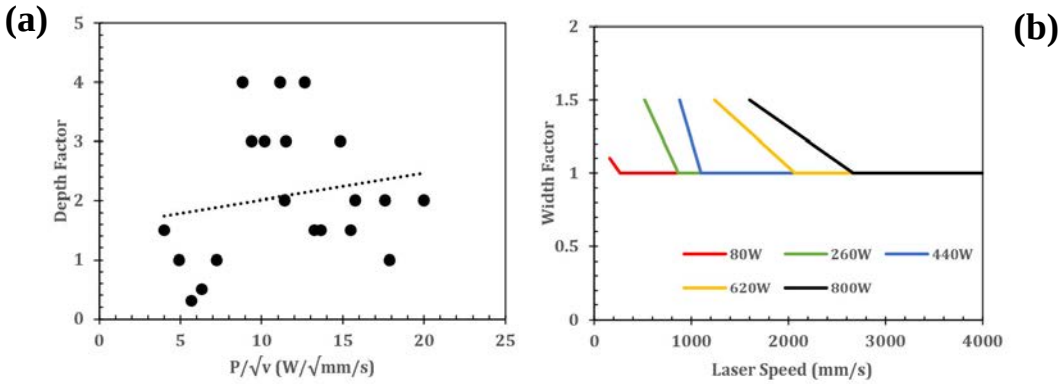


**Figure 4.** Enhancement factor plots **(a)** Along depth **(b)** Along width.

**Table 1.** Enhancement factors' coefficient values along depth and width.

| $a_1$ | $b_1$ | $a_2$ | $b_2$ | $v_a$ | |
|---|---|---|---|---|---|
| 0.0453 | 1.5652 | | | | **Laser Power (W)** |
| | | -0.0009 | 1.25 | 266.67 | **80** |
| | | -0.0014 | 2.25 | 866.67 | **260** |
| | | -0.0023 | 3.5 | 1100 | **440** |
| | | -0.0006 | 2.37 | 2066.67 | **620** |
| | | -0.0003 | 2.1 | 2666.67 | **800** |

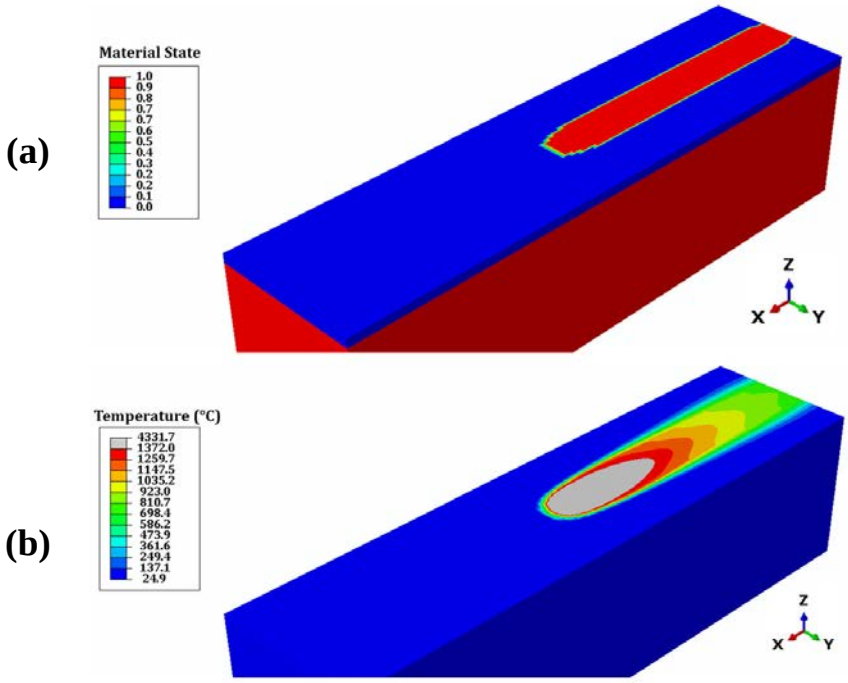


**Figure 5.** Contour plot during SLM process. **(a)** Material State contour **(b)** Temperature contour.

**Figure 5-(a)** illustrates the material state contour in the SLM simulation. The powder state is shown in blue color whereas solid and liquid states are shown in red color.

Although liquid and solid states have the same index, conduction inside the melt pool is being enhanced separately using the anisotropically enhancement factors. The area affected by the enhancement factors is shown in **Figure 5-(b)** which shows the temperature contour with the grey color representing the melt pool.

USDFLD subroutine and field-dependent data have been effectively utilized for modeling the SLM process in ABAQUS. However, utilizing this subroutine as a means to simulate the state transition, makes it such that the reference temperature for phase transition is the temperature at the beginning of the increment. This causes the phase transition to be consistently lagging by a single time increment relative to the applied heat source as demonstrated by Tangestani et al. [33]. The effect of this phenomenon becomes significant for the HL heat input model as the time increments are large. A solution was proposed by Tangestani et al. [33] using the energy absorption but it's not a practical one when it comes to predicting the molten pool geometry accurately. UMATHT allows the user to have access to the temperature increment as well as temperature at the beginning of the increment which could be used to calculate the temperature at the end of the increment. By using this temperature as the phase transition reference, the phase transition problem could be solved. Necessary number of iterations must be allowed to achieve equilibrium within the HL model. This is due to severe non-linearity in a single time increment.

The density used belongs to the current state of the material as well which helps to further improve the thermal history predictions when utilizing the UMATHT subroutine as demonstrated by Jeong et al. [37].

## 4. RESULTS & DISCUSSION

### 4.1. MELT POOL GEOMETRY ANALYSIS

The laser radius of 100μm and an absorption coefficient (η) of 0.36 was chosen based on works done in the literature [34, 38]. **Figure 6-(A)** through **Figure 6-(J)** show the melt pool dimensions predicted by simulation compared experimentally in different process parameters. The error margin denotes the uppermost and lowermost values recorded during the experimental observations.

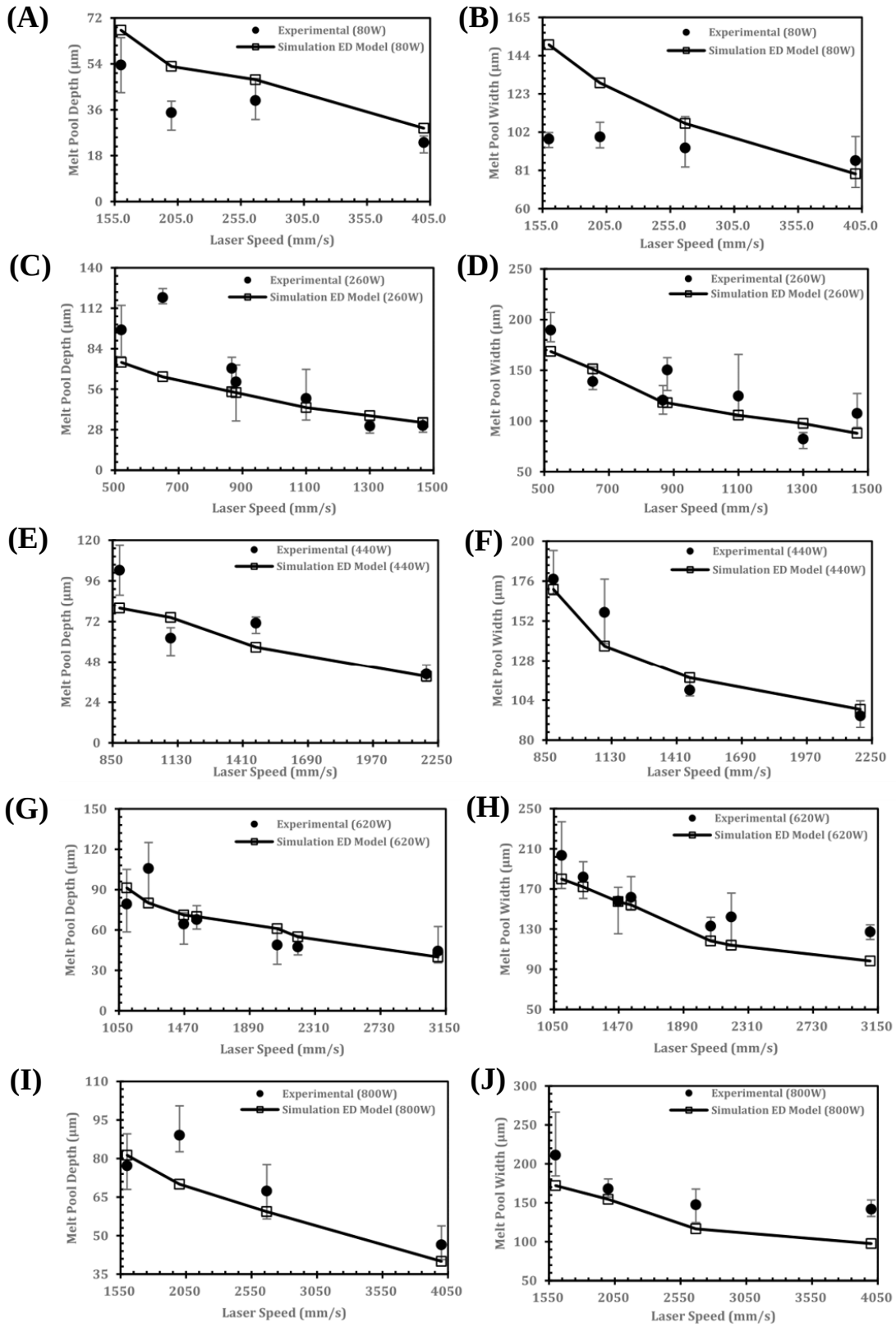


**Figure 6.** Melt pool dimensions comparison between experimental and ED model in different Laser speeds and powers. **(A)** and **(B)** 80W, **(C)** and **(D)** 260W, **(E)** and **(F)** 440W, **(G)** and **(H)** 620W and **(I)** and **(J)** 800W.

**Table 2** demonstrates the average rate at which the melt pool dimensions change with altering laser parameters. The change rates are presented 100 times bigger than the nominal value to have a more sensible physical meaning. This means the values are presented as the laser power or laser speed increase by 100W or 100mm/s.

Using the experimental results, it's concluded that melt pool width and depth increase at an average rate of $19.33\frac{\mu m}{W}$ and $11.07\frac{\mu m}{W}$ with laser power. However, the dimensions decrease at an average rate of $5.832\frac{\mu m}{W}$ and $5.75\frac{\mu m}{W}$ with laser speed. This deduction demonstrates that laser power exerts a notably more substantial influence on melt pool size when compared to laser speed. This result is consistent with the conclusions achieved by other researchers [31].

The aspect ratio of the experimentally printed melt pools has also been analyzed which is an indication of the heat transfer mode inside the molten pool. With lower values having the conduction mode and the higher values having the convection (keyhole) mode. The shift from conduction to convection mode typically takes place when aspect ratio values reach 0.5 or exceed this threshold for SS316L [39]. **Figure 7-(a)** illustrates a scatter plot which indicates melt pool dimensions for various laser parameters. The parameters are categorized based on energy density levels. The data sets which don't have particular energy densities are marked as "Random Energy Density". With the dashed line having a slope of 0.5, the points above the line can be categorized as keyhole heat transfer and the points below as conduction heat transfer mode.

The heat transfer mode can be confirmed using the molten pool geometry. When bell-shaped melt pools are observed, the heat transfer is governed by convection. When shallow and wide molten pool shapes are observed, the heat transfer is governed by conduction. **Figure 7-(b)** illustrates an experimental bell-shaped molten pool geometry. **Figure 8** illustrates the simulated melt pool having the same bell shape geometry which establishes the conclusion that the FEM model possesses the capability to precisely forecast melt pool geometry when the dominant heat transfer mode is governed by convection in the process.

**Table 2.** Average melt pool width and depth change rate with laser parameters increase.

| | **Change Rate with Laser Speed** | | **Change Rate with Laser Power** | |
|---|---|---|---|---|
| | 100×Width ($\frac{\mu m}{mm/s}$) | 100× Depth ($\frac{\mu m}{mm/s}$) | 100× Width ($\frac{\mu m}{W}$) | 100× Depth ($\frac{\mu m}{W}$) |
| **Experimental** | -5.832 | -5.75 | 19.33 | 11.07 |
| **ED Model** | -9.856 | -5.248 | 19.507 | 11.82 |
| **HL Model** | -11.172 | -6.878 | 17.485 | 11.645 |

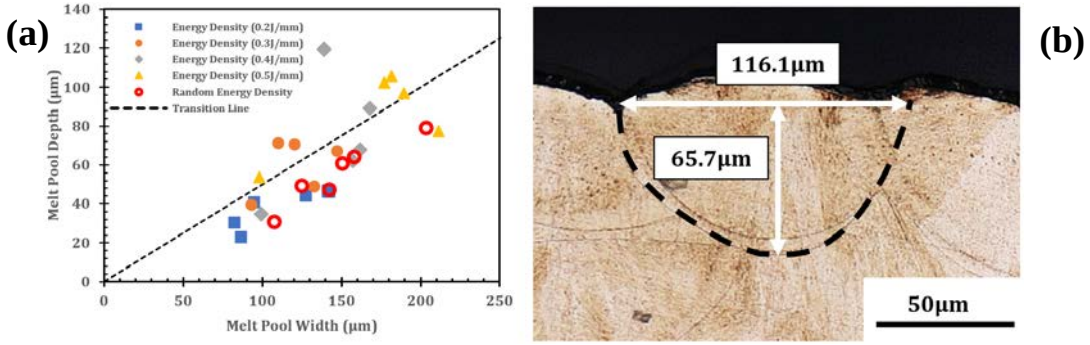


**Figure 7. (a)** Molten pool dimension scatter plot **(b)** Bell shape melt pool cross section with aspect ratio of 0.52.

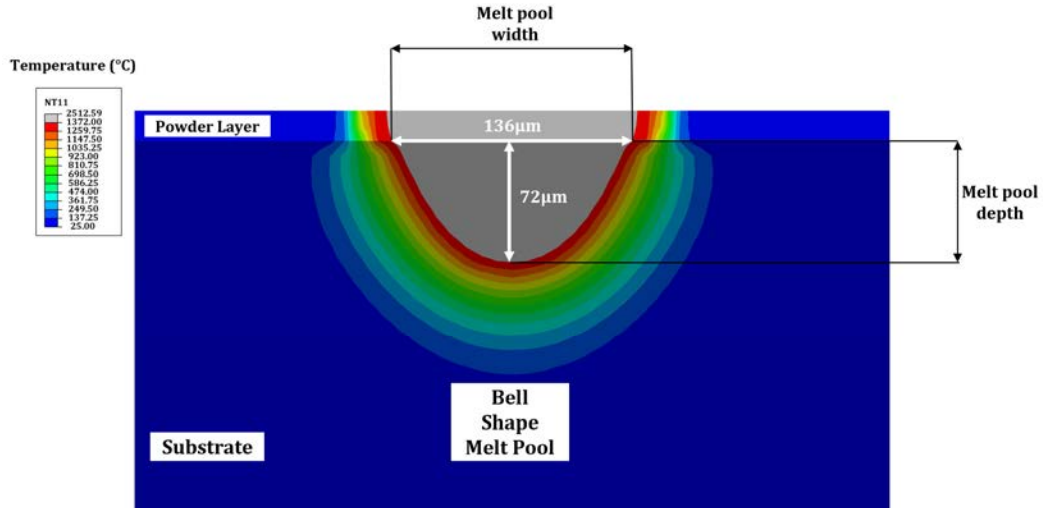


**Figure 8.** Simulated molten pool showing a bell shape dimension for the melt pool geometry.

### 4.2. ED MODEL EVALUATION

The approach employed to compute the dimensions of the molten pool generated in the simulation is adopted from the existing literature [33, 40]. The cross-sectional shape of the molten pool is established by adjusting the contour range, wherein the maximum contour value is designated as the melting temperature. Following the extraction of the cross-section, the width and depth are measured and compared with the experimental results. The dimensions are illustrated in **Figure 8**.

**Figure 6** illustrates the disparity between the experimental and simulated results. In constant laser power, the melt pool dimensions must decrease as the laser speed increases which can be seen for the simulated results. However, not all experimental data follow this trend which is caused due to experimental errors during the SLM process.

The average rate at which melt dimensions increase with respect to laser power increase is $19.507\frac{\mu m}{w}$ and $11.82\frac{\mu m}{w}$. Conversely the average decrease rate with respect to the laser speed increase is $6.174\frac{\mu m}{w}$ and $6.08\frac{\mu m}{w}$ which matches the experimental results. The average difference regarding the melt pool width and depth is 16μm and 10μm. This deviation is acceptable due to the error margin present in the experimental results. We can affirm that the results obtained are reliable, and the model can be relied upon for predicting the geometrical characteristics of the melt pools formed during the process.

### 4.3. HL MODEL CALIBRATION

According to Irwin et al. [31] the time increment is defined in terms of parameter τ which represents the laser travel distance with respect to the laser spot diameter. The representation is as follows:

$$\tau = \frac{v_s \Delta T}{r_l} \quad (13)$$

Where $v_s$ is laser speed, $r_l$ denotes radius of laser while $\Delta T$ represents time increment. According to **Eq.13**, τ represents the distance laser travels in each increment compared to the laser radius. For instance, if τ=5, the travel distance of the laser is 5 times the laser radius in a single increment which will lead to significant simulation time reduction. The ED model is used as a reference for the calibration of the HL model as discussed by Tangestani et al. [33]. In order to achieve this, the "C" parameter is adjusted in a manner that minimizes the error in dimension prediction of the molten pool in HL and ED model. The cross section consisting of the largest liquid region is considered as the reference section in the HL model. To do so, a python script was developed to approximate the maximum width and depth value based on the melting temperature. The "C" parameter is configured to a value of 1.5 as it demonstrates the highest level of concordance with the ED model. The dependence of "C" parameter on time increment has not been considered. So, we are assuming a fixed travel distance of 5 times the laser radius throughout the simulation. Hence, it's obvious that if τ≠5, then the chosen "C" parameter will make the model either accommodate extra heat (τ<5) or less heat (τ>5). This issue was avoided by carefully choosing the number of iterations.

### 4.4. HL MODEL EVALUATION

#### 4.4.1. MELT POOL GEOMETRY ANALYSIS

First the molten pool geometry is validated with the ED model and the experimental data. **Figure 9-(A)** through **Figure 9-(J)**, illustrate molten pool dimensions comparison between the two models and experimental data. The figures show trend of melt pool dimensions with respect to laser speed in different laser power values. First the two models are compared with each other.

The greatest disparity between the two models in terms of width and depth values amounts to 11μm and 6μm, respectively. The mean discrepancies between the two models are approximately 5μm for both width and depth, indicating a degree of consistency between the ED and HL models.

The average change rate of melt pool dimensions in the HL model has also been investigated. The increase rate of width and depth with respect to laser power is $17.485\frac{\mu m}{w}$ and $11.645\frac{\mu m}{w}$. The decrease rate with respect to laser speed is $7.19\frac{\mu m}{w}$ and $7.968\frac{\mu m}{w}$.

When comparing the HL model experimentally, the average deviations for width and depth are approximately 20μm and 9μm, respectively. The results are just a bit divergent compared to the ED model. Still the error margin of the experimental data is met. The deduction affirms that the HL model is equally precise as the ED model but offers enhanced efficiency.

The results also conclude that the use of the anisotropic model in conjunction with the HL model is able to reach acceptable error margin for both width and depth directions. This was not the case for the work conducted by Tangestani et al. [33] where although the model showed acceptable agreement for depth of the molten pool, the accuracy dropped drastically for width of the melt pool. This could lead to errors regarding some applications such as component porosity measurements where precise melt pool geometries are required.

#### 4.4.2. COMPUTATIONAL COST

The HL model is more time efficient compared to the ED model [30, 31]. The simulation time is predominantly determined by the quantity of increments and iterations. The ED model demands a substantial number of increments which results in extended computational time. The developed HL model requires small number of increments but in return larger number of iterations to reach equilibrium criteria within the elements during the analysis. An average of about 40 number of iterations are needed for the equilibrium criteria to be met in each increment. On average, HL model exhibits a computational speed that is approximately 100 times faster than that of the ED model.

#### 4.4.3. MATERIAL STATE

The importance of the HL model becomes particularly evident when modeling component-sized models, where the use of beam-scale heat inputs is not feasible. Modeling the porosity within the component is one of these cases where precise prediction of the material state during the analysis is required. The next section focuses on material state comparison between ED and HL model.

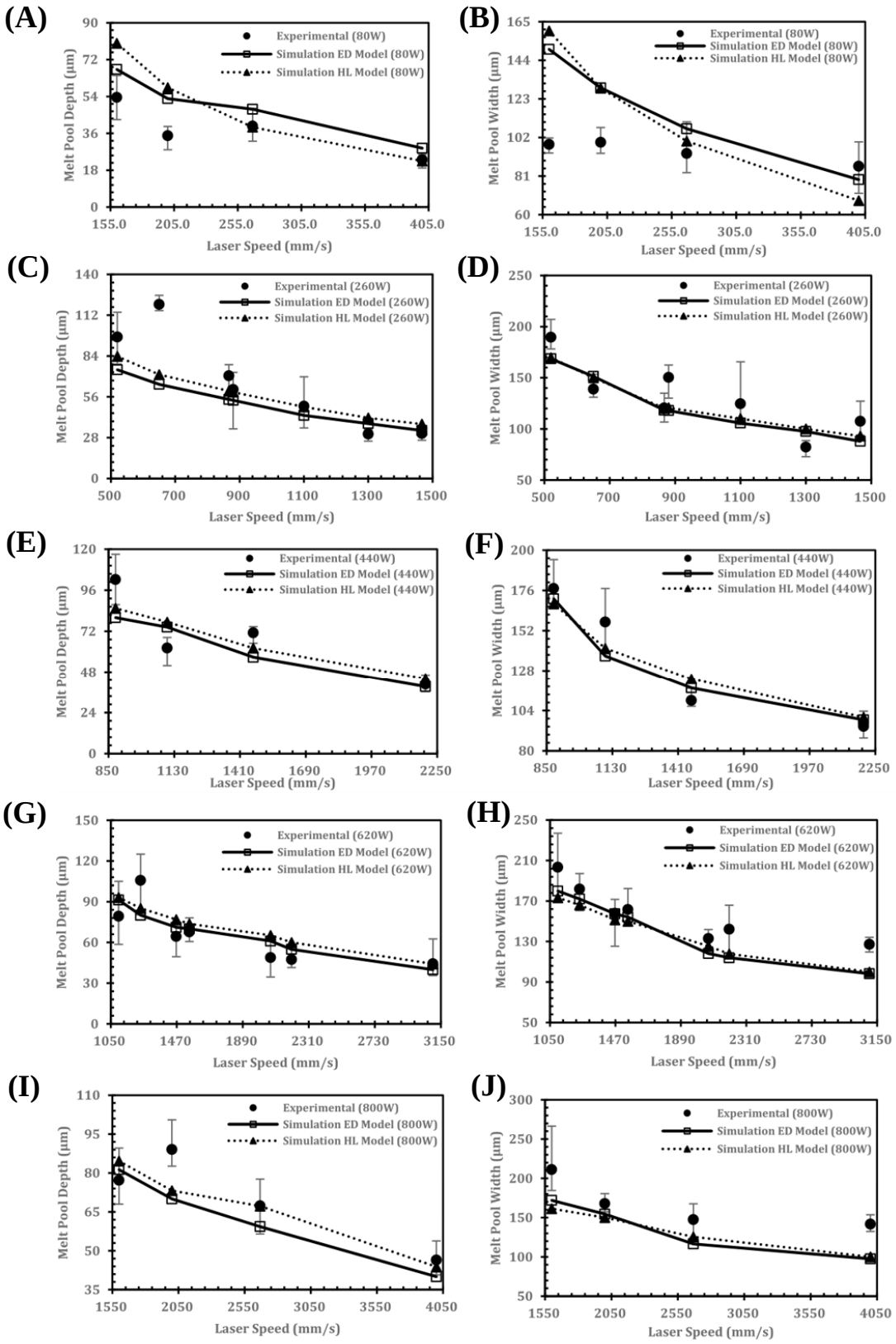


**Figure 9.** Melt pool dimensions comparison between experimental, ED model and HL model in different Laser speeds and powers. **(A)** and **(B)** 80W, **(C)** and **(D)** 260W, **(E)** and **(F)** 440W, **(G)** and **(H)** 620W and **(I)** and **(J)** 800W.

To compare the material state between the two models, a python script is developed which counts the number of solid-state integration points in the powder layer of the single track. This indicates the number of elements which undergo phase transition during the simulation. This number can then act as a reference to compare the error regarding the material state in the two models.

**Figure 10-(A)** and **Figure 10-(B)** show the comparison of number of solid-state integration points in the single-track model for the ED and the HL model. These figures are presented for the worst case (80W) and the best case (440W) regarding the errors.

**Figure 10-(C)** illustrates the error present between the two models. It is concluded that the highest error regarding the worst case is 20%. The data for the best case all fall below 10%. The reason for this error rise in the 80W case is analyzed in the following.

No matter how well the HL model is calibrated, there will always be an error present in the material state between the two models. This occurs due to small time increments in the ED model, which allows the largest cross-section of the melt pool to exert its influence across the entire geometry. but the same can't be said about the HL model.

In calibration of the track-scale, the largest cross section was used to calibrate the HL model with respect to the ED model. This means that only the calibrated cross section is identical to the ED model. However, when moving away from calibrated cross section, the dimensions progressively diminish until reaching the laser's initial point at the start of the increment. Hence, the deviation is caused.

This in particular affects the HL model in lower laser power values for the melt pool dimensions are generally smaller, hence the melt pool dimensions collapse faster in the HL model. This is the main cause of error for the 80W case illustrated in **Figures 10-(C).**

A possible solution is to use a smaller cross section as the reference for the HL model which could lead to over estimation of the temperature history and melt pool geometries.

Though the formation of error is inevitable, the average error percentage regarding the material state transition in all cases is about 10% which yields acceptable accuracy with regards to the ED model.

#### 4.4.4. SINGLE-TRACK TEMPERATURE

Analyzing the track temperature during the simulation is an important criteria of crack formation during SLM process. This is because material undergoes phase transition and solidifies which determines the possibility of crack formation during the process. As a result, temperature history during the process must be compared between ED and HL model. To do so, nodal temperatures along scan direction are compared. The top surface of the substrate has been chosen as the reference between the two models for the comparison which would lead to comparison of melt pool length as well as the temperature history.

Temperature history is exported for four different process parameters having energy densities of 0.2, 0.3, 0.4 and 0.5 J/mm. The laser power is kept a constant of 260W and four different laser speeds have been considered. The nodal temperatures along the laser path at the top of the substrate are shown in **Figure 11-(A)** through **Figure 11-(D).** As energy density increases, the maximum temperature experienced during the process rises as well.

As was reported by Tangestani et al. [33] the HL model does not predict the maximum temperature reached in ED model for heat input is integrated over time increment. An average error of 15% is concluded between the two models regarding maximum temperature.

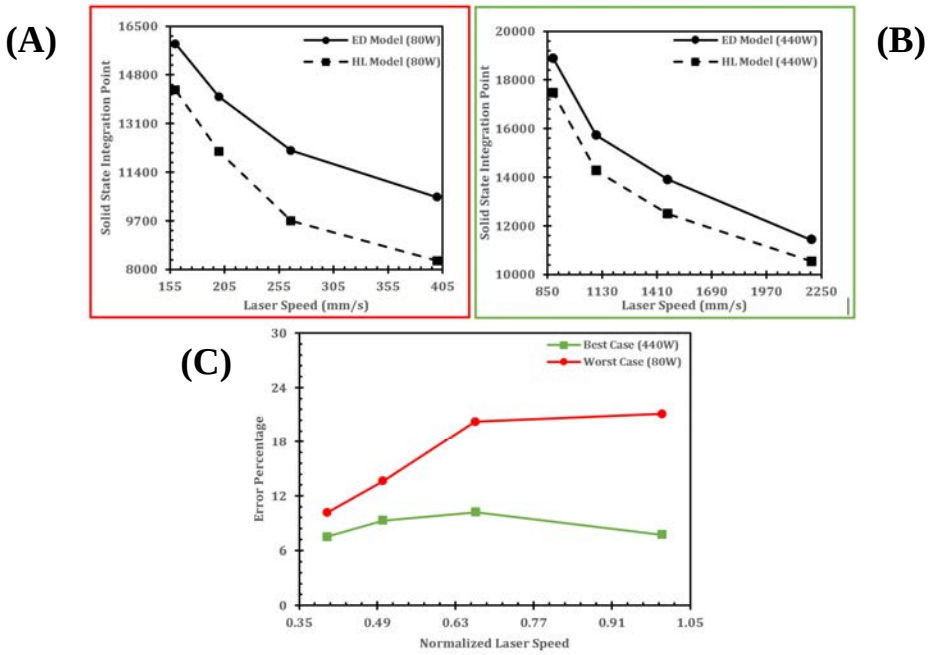


**Figure 10.** Number of integration points comparison between ED and HL model for **(A)** worst case (80W) and **(B)** best case (440W). **(C)** Error percentage between ED and HL model for worst and best case.

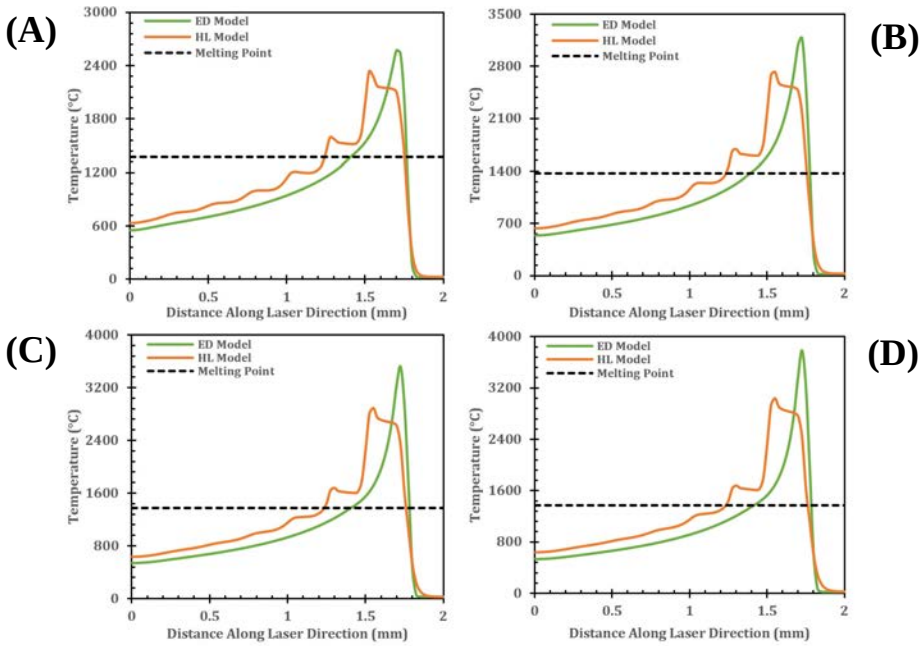


**Figure 11.** Comparison of nodal temperature along laser path between the Ed and HL model. Laser power 260W and laser speeds **(A)** 1300mm/s **(B)** 866mm/s **(C)** 650mm/s **(D)** 520mm/s.

As for the melt pool length, the horizontal line represents the melting point of the SS316L and the portion above the line represents the melted region. The results conclude that melt pool length average error is about 35%. This is attributed to gradual but modest increase in temperature profile illustrated in **Figure 11-(A)** through **Figure 11-(D)**.

Another aspect of temperature history that we've examined is how the models perform when melt pool begins to solidify. As temperature drops, the two plots start to converge. The error is calculated around 1372°C which is about the temperature where solidification occurs and is a critical point for micro cracking initiation. An average error of 13% is calculated between the two models in the range of 1350 to 1400°C.

#### 4.4.5. COOLING RATE

Cooling rate governs grain size during solidification, consequently leading to thermal stresses in the fabricated components. [35]. Therefore, the rate at which the part is cooled needs to be captured accurately. **Figure 12-(A)** through **(D)**, show the cooling rates of the ED model in comparison with the HL model.

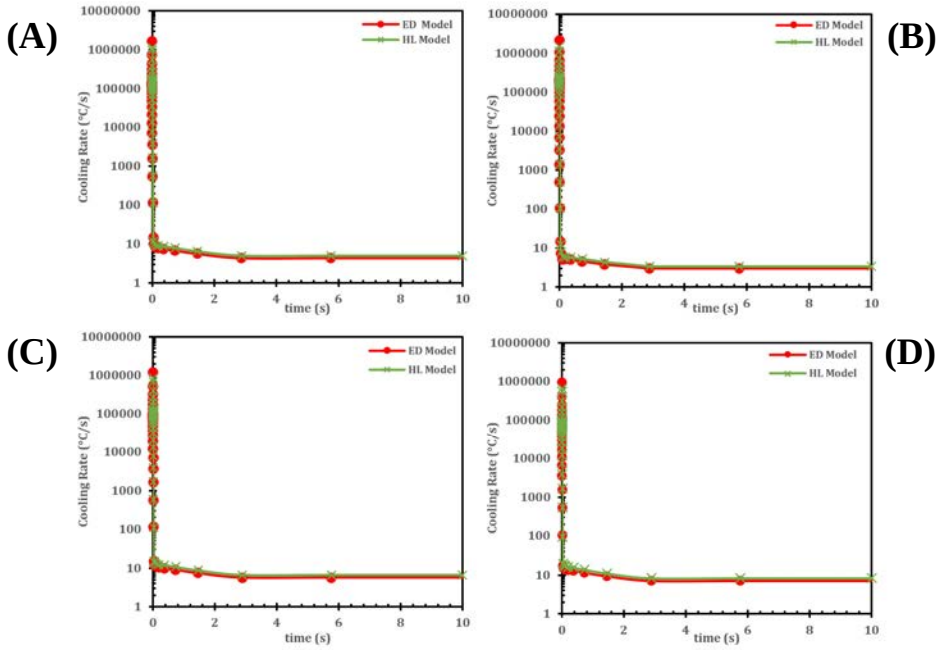


**Figure 12.** Comparison of cooling rates. Laser power 260W and laser speed **(A)** 1300mm/s **(B)** 866mm/s **(C)** 650mm/s **(D)** 520mm/s.

The same parameters as **Figure 11** were considered. Melt pool boundary is chosen as case of study for it's a critical point in crack formation. The maximum cooling rate is in order of $10^6$°C/s which is consistent with results reported by Liu et al. [35].
**Figure 12** also illustrates cooling rate decreases rapidly until it reaches the steady state around 3°C/s to 7°C/s with increasing energy density after about 1 sec. It can also be inferred that augmenting the laser speed results in an increase in the maximum cooling rate. This is attributed to the shorter time intervals between each pass of the laser through the material.

## 5. CONCLUSION

In this paper, the well stablished track-scale model is used in conjunction with the anisotropic thermal conduction model to develop an efficient yet accurate material model which is able to predict temperature history and melt pool dimensions in a wide range of process parameters with acceptable precision in the SLM process. A solution to the phase transition problem during simulation of LPBF process while using track-scale model is provided and the calibration methodology of the anisotropic thermal conduction is presented.
First ED model was validated experimentally regarding melt pool dimensions. The results showed that average difference is 16µm and 10µm in width and depth while capturing the error margin in almost all of the experimental cases. ED and HL model are compared in terms of melt pool geometry, computational time, material phase transition, temperature profile and cooling rate. A conclusion of the results obtained is as follows

1- The melt pool dimensions comparison conclude that the two models have an average difference of about 5µm which yields a significant improvement compared with the previous work done on track-scale model of LPBF process.

2- In average HL model is about 100 times faster than ED model which makes it more efficient.

3- Material transition comparison during the process concludes that the maximum error between the two models is about 20% which occurs in the lowest laser power level. The average error is about 10% which makes the HL model a viable substitute.

4- Temperature profile comparison yields an average reduction of 15% regarding the maximum temperature in the HL model while yielding an average increase of 35% regarding melt pool length during simulation. The temperature after cooling was compared around the solidification temperature. An average error of 13% was concluded around the solidus temperature.

5- Cooling rate analysis yields values in order of $10^6$°C/s which is close to values reported by researchers. The cooling rate reaches steady state values after about 1 sec. The steady state cooling rate values increase with respect to the energy density implemented. The initial cooling rate values increase by increasing the laser speed due to smaller time intervals.

6- The HL model is also compared to the experimental results. An average difference of 20µm in width and 9µm is concluded while capturing the error margin in almost all of the experimental cases, same as the ED model. Concluding that the HL model can now be a viable substitute for the ED model which makes the simulations more efficient yet maintaining accuracy which can be used in component scale models.

## Acknowledgements

The authors would like to thank Carpenter Technology Cooperation for supplying the powder material used in this study.

## REFRENCES

1. Liu, J., et al., *Achieving Ti6Al4V alloys with both high strength and ductility via selective laser melting.* Materials Science and Engineering: A, 2019. **766**: p. 138319 DOI: https://doi.org/10.1016/j.msea.2019.138319.
2. Miranda, G., et al., *A study on the production of thin-walled Ti6Al4V parts by selective laser melting.* Journal of Manufacturing Processes, 2019. **39**: p. 346-355 DOI: https://doi.org/10.1016/j.jmapro.2018.12.036.
3. Lo, Y.-L., B.-Y. Liu, and H.-C. Tran, *Optimized hatch space selection in double-scanning track selective laser melting process.* The International Journal of Advanced Manufacturing Technology, 2019. **105**(7): p. 2989-3006 DOI: https://doi.org/10.1007/s00170-019-04456-w.
4. Wang, Z., et al., *Optimization of processing parameters and establishment of a relationship between microstructure and mechanical properties of SLM titanium alloy.* Optics & Laser Technology, 2019. **112**: p. 159-167 DOI: https://doi.org/10.1016/j.optlastec.2018.11.014.
5. Ali, H., H. Ghadbeigi, and K. Mumtaz, *Effect of scanning strategies on residual stress and mechanical properties of Selective Laser Melted Ti6Al4V.* Materials Science and Engineering: A, 2018. **712**: p. 175-187 DOI: https://doi.org/10.1016/j.msea.2017.11.103.
6. Drücker, S., et al., *Experimental and numerical mechanical characterization of additively manufactured Ti6Al4V lattice structures considering progressive damage.* International Journal of Mechanical Sciences, 2021. **189**: p. 105986 DOI: https://doi.org/10.1016/j.ijmecsci.2020.105986.
7. Khorasani, A., et al., *The effect of SLM process parameters on density, hardness, tensile strength and surface quality of Ti-6Al-4V.* Additive Manufacturing, 2019. **25**: p. 176-186 DOI: https://doi.org/10.1016/j.addma.2018.09.002.
8. Liu, B., et al., *Numerical investigation on heat transfer of multi-laser processing during selective laser melting of AlSi10Mg.* Results in Physics, 2019. **12**: p. 454-459 DOI: https://doi.org/10.1016/j.rinp.2018.11.075.
9. Ming, W., et al., *Dynamic mechanical properties and machinability characteristics of selective laser melted and forged Ti6Al4V.* Journal of Materials Processing Technology, 2019. **271**: p. 284-292 DOI: https://doi.org/10.1016/j.jmatprotec.2019.04.015.
10. Aboulkhair, N.T., et al., *On the formation of AlSi10Mg single tracks and layers in selective laser melting: Microstructure and nano-mechanical properties.* Journal

of Materials Processing Technology, 2016. **230**: p. 88-98 DOI: https://doi.org/10.1016/j.jmatprotec.2015.11.016.
11. Qi, T., et al., *Selective laser melting of Al7050 powder: Melting mode transition and comparison of the characteristics between the keyhole and conduction mode.* Materials & Design, 2017. **135**: p. 257-266 DOI: https://doi.org/10.1016/j.matdes.2017.09.014.
12. Zhang, H., et al., *Effect of Zirconium addition on crack, microstructure and mechanical behavior of selective laser melted Al-Cu-Mg alloy.* Scripta Materialia, 2017. **134**: p. 6-10 DOI: https://doi.org/10.1016/j.scriptamat.2017.02.036.
13. Cherry, J.A., et al., *Investigation into the effect of process parameters on microstructural and physical properties of 316L stainless steel parts by selective laser melting.* The International Journal of Advanced Manufacturing Technology, 2015. **76**(5): p. 869-879 DOI: https://doi.org/10.1007/s00170-014-6297-2.
14. He, B., et al., *Rigid-flexible coupling virtual prototyping-based approach to the failure mode, effects, and criticality analysis.* 2019 DOI: https://doi.org/10.1007/s00170-018-2641-2.
15. Mazur, M., et al., *Deformation and failure behaviour of Ti-6Al-4V lattice structures manufactured by selective laser melting (SLM).* The International Journal of Advanced Manufacturing Technology, 2016. **84**(5): p. 1391-1411 DOI: https://doi.org/10.1007/s00170-015-7655-4.
16. Wang, D., et al., *Research on the fabricating quality optimization of the overhanging surface in SLM process.* The International Journal of Advanced Manufacturing Technology, 2012. **65** DOI: https://doi.org/10.1007/s00170-012-4271-4.
17. Simson, T., et al., *Residual stress measurements on AISI 316L samples manufactured by selective laser melting.* Additive Manufacturing, 2017. **17**: p. 183-189 DOI: https://doi.org/10.1016/j.addma.2017.07.007.
18. Hussein, A., et al., *Advanced lattice support structures for metal additive manufacturing.* Journal of Materials Processing Technology, 2013. **213**(7): p. 1019-1026 DOI: https://doi.org/10.1016/j.jmatprotec.2013.01.020.
19. Denlinger, E., J. Heigel, and P. Michaleris, *Residual stress and distortion modeling of electron beam direct manufacturing Ti-6AL-4V.* Proc Inst Mech Eng B: J Eng Manuf, 2014. **229** DOI: https://doi.org/10.1177/0954405414539494.
20. Yilbas, B. and S. Akhtar, *Laser Welding of AISI 316 Steel: Microstructural and Stress Analysis.* Journal of Manufacturing Science and Engineering, 2013. **135** DOI: https://doi.org/10.1115/1.4024155.
21. Dai, D. and D. Gu, *Effect of metal vaporization behavior on keyhole-mode surface morphology of selective laser melted composites using different protective atmospheres.* Applied Surface Science, 2015. **355**: p. 310-319 DOI: https://doi.org/10.1016/j.apsusc.2015.07.044.
22. Dai, K. and L. Shaw, *Finite element analysis of the effect of volume shrinkage during laser densification.* Acta Materialia, 2005. **53**(18): p. 4743-4754 DOI: https://doi.org/10.1016/j.actamat.2005.06.014.
23. Yuan, P. and D. Gu, *Molten pool behaviour and its physical mechanism during selective laser melting of TiC/AlSi10Mg nanocomposites: Simulation and experiments.* Journal of Physics D: Applied Physics, 2015. **48**: p. 035303 DOI: https://doi.org/10.1088/0022-3727/48/3/035303.
24. Kamara, M., et al., *Modelling of the Melt Pool Geometry in the Laser Deposition of Nickel Alloys Using the Anisotropic Enhanced Thermal Conductivity Approach.* Proceedings of the Institution of Mechanical Engineers Part B Journal of Engineering Manufacture, 2011. **225** DOI: https://doi.org/10.1177/09544054JEM2129.
25. Safdar, S., et al., *An anisotropic enhanced thermal conductivity approach for modelling laser melt pools for Ni-base super alloys.* Applied mathematical modelling, 2013. **37**(3): p. 1187-1195 DOI: https://doi.org/10.1016/j.apm.2012.03.028.
26. Siao, Y.-H. and C.-D. Wen, *Thermal analysis of anisotropic heat conduction model with experimental validation on molten pool during selective laser melting.* Materials Today Communications, 2021. **27**: p. 102425 DOI: https://doi.org/10.1016/j.mtcomm.2021.102425.
27. Gouge, M., et al., *Experimental Validation of Thermo-mechanical Part-Scale Modeling for Laser Powder Bed Fusion Processes.* Additive Manufacturing, 2019. **29** DOI: https://doi.org/10.1016/j.addma.2019.06.022.
28. Cook, P.S. and A.B. Murphy, *Simulation of melt pool behaviour during additive manufacturing: Underlying physics and progress.* Additive manufacturing, 2020. **31**: p. 100909 DOI: https://doi.org/10.1016/j.addma.2019.100909.
29. Mukherjee, T., W. Zhang, and T. DebRoy, *An improved prediction of residual stresses and distortion in additive manufacturing.* Computational Materials Science, 2017. **126**: p. 360-372 DOI: https://doi.org/10.1016/j.commatsci.2016.10.003.
30. Luo, Z. and Y. Zhao, *Numerical simulation of part-level temperature fields during selective laser melting of stainless steel 316L.* The International Journal of Advanced Manufacturing Technology, 2019. **104**(5): p. 1615-1635 DOI: https://doi.org/10.1007/s00170-019-03947-0.
31. Irwin, J. and P. Michaleris, *A Line Heat Input Model for Additive Manufacturing.* 2015. **1** DOI: https://doi.org/10.1115/MSEC20159240.
32. Cheng, B., S. Shrestha, and K. Chou, *Stress and deformation evaluations of scanning strategy effect in selective laser melting.* Additive Manufacturing, 2016. **12**: p. 240-251 DOI: https://doi.org/10.1016/j.addma.2016.05.007.
33. Tangestani, R., et al., *An Efficient Track-Scale Model for Laser Powder Bed Fusion Additive Manufacturing: Part 1 - Thermal Model.* Frontiers in Materials, 2021. **8**: p. 753040 DOI: https://doi.org/10.3389/fmats.2021.753040.
34. Waqar, S., K. Guo, and J. Sun, *FEM analysis of thermal and residual stress profile in selective laser melting of 316L stainless steel.* Journal of Manufacturing Processes, 2021. **66**: p. 81-100 DOI: https://doi.org/10.1016/j.jmapro.2021.03.040.
35. Liu, S., et al., *Microstructure prediction of selective laser melting AlSi10Mg using finite element analysis.* Materials & Design, 2018. **142**: p. 319-328 DOI: https://doi.org/10.1016/j.matdes.2018.01.022.
36. Zhang, Z., et al., *3-Dimensional heat transfer modeling for laser powder-bed fusion additive manufacturing with*

*volumetric heat sources based on varied thermal conductivity and absorptivity*. Optics & Laser Technology, 2019. **109**: p. 297-312 DOI: https://doi.org/10.1016/j.optlastec.2018.08.012.

37. Jeong, S.H., et al., *Thermal Analysis for Simulation of Metal Additive Manufacturing Process Considering Temperature- and History-Dependent Material Properties.* International Journal of Aeronautical and Space Sciences, 2021. **22**(1): p. 52-63 DOI: https://doi.org/10.1007/s42405-020-00283-6.
38. Heeling, T., M. Cloots, and K. Wegener, *Melt pool simulation for the evaluation of process parameters in selective laser melting.* Additive Manufacturing, 2017. **14**: p. 116-125 DOI: https://doi.org/10.1016/j.addma.2017.02.003.
39. Aggarwal, A., S. Patel, and A. Kumar, *Selective Laser Melting of 316L Stainless Steel: Physics of Melting Mode Transition and Its Influence on Microstructural and Mechanical Behavior*. JOM, 2018. **71** DOI: https://doi.org/10.1007/s11837-018-3271-8.
40. Dong, Z., et al., *Effect of Hatch Spacing on Melt Pool and As-built Quality During Selective Laser Melting of Stainless Steel: Modeling and Experimental Approaches.* Materials, 2019. **12**(1): p. 50 DOI: https://doi.org/10.3390/ma12010050.